SIAM Review
Vol. 63, No. 1, pp. 100–120

The Dynamics of Bilateral Olfactory Search and Navigation*

Nour Riman†
Jonathan D. Victor‡
Sebastian D. Boie‡
Bard Ermentrout§

Abstract. Animals use stereo sampling of odor concentration to localize sources and follow odor trails. We analyze the dynamics of a bilateral model that depends on the simultaneous comparison between odor concentrations detected by left and right sensors. The general model consists of three differential equations for the positions in the plane and the heading. When the odor landscape is an infinite trail, we reduce the dynamics to a planar system whose dynamics has just two fixed points. Using an integrable approximation (for short sensors) we estimate the basin of attraction. In the case of a radially symmetric landscape, we again can reduce the dynamics to a planar system, but the behavior is considerably richer with multistability, isolas, and limit cycles. As in the linear trail case, there is also an underlying integrable system when the sensors are short. In odor landscapes that consist of multiple spots and trail segments, we find periodic and chaotic dynamics and characterize the behavior on trails with gaps and trails that turn corners.

Key words. stereo sampling, tropotaxis, olfactory navigation, nonlinear dynamics

AMS subject classifications. 00A69, 37N25, 92D50

DOI. 10.1137/19M1265934

1. Introduction.

Animals use olfactory cues to navigate through their environment in order to find food, encounter mates, avoid predators, and locate their home. This requires an ability to both localize odor sources and follow odor trails. To localize odor, animals have been observed to use serial sampling (klinotaxis) or bilateral sampling (tropotaxis) of the concentration [23]. Serial sampling depends on intersniff comparisons of odor concentrations between sequential sniffs that are measured at different locations. Bilateral sampling, on the other hand, depends on comparisons of odor concentrations detected by sensors located at two different positions of the body.

*Received by the editors June 3, 2019; accepted for publication (in revised form) April 21, 2020; published electronically February 4, 2021.
https://doi.org/10.1137/19M1265934
Funding: The work of the first and fourth authors was supported by the NSF through grant PHY1555916. The work of the second and third authors was supported by the NSF through grant IOS1555891.

†Neuroscience Institute, Carnegie Mellon University, Pittsburgh, PA 15213 USA, and Center for the Neural Basis of Cognition, Carnegie Mellon University, Pittsburgh, PA 15213 USA (nourr@andrew.cmu.edu).
‡Feil Family Brain and Mind Research Institute, Weill Cornell Medical College, New York, NY 10065 USA (jdvicto@med.cornell.edu, sebboie@mailbox.org).
§Department of Mathematics, University of Pittsburgh, Pittsburgh, PA 15260 USA, and Center for the Neural Basis of Cognition, Carnegie Mellon University, Pittsburgh, PA 15213 USA (bard@pitt.edu).

The ability to use intersensor geometry to localize odors has been observed in many animals, especially insects. When one of the antennas is removed, walking fruit flies (*Drosophila melanogaster*) [3], flying fruit flies [10], ants (*Lasius fuliginosus*) [12], and honeybees (*Apis mellifera*) [19] show a tendency to orient toward the intact side. Marine animals have also shown dependence on bilateral information of the odor concentration to orient. Leopard sharks [20], which are nearshore species, follow more tortuous paths and end farther away from the shore when one of their nostrils is blocked, in contrast to control sharks which end closer to the shore with relatively straight tracks. Crustaceans also exhibit a loss of ability to correctly orient in an odor plume and efficiently find odor sources when one of their antennules is ablated [1, 8, 11, 17, 24]. The detriment of loss of bilateral inputs has also been shown in mammals. When one of the nostrils is partially or completely blocked, rats' accuracy in localizing odor drops significantly and their response is biased toward the unblocked side. Their performance in tracking odor trails also declines and is less efficient[14, 23]. Blocking a nostril in moles also biases the animal in one direction and increases the latency to find the sources [6]. In this study, crossing the airflow, by inserting polyethylene tubes into the nostrils, disrupts the ability to localize sources. Likewise, human subjects' accuracy almost halves when one nostril is taped during a scent tracking task [22].

Due to the behavioral and neural [15, 21, 23] evidence of the importance of bilateral comparisons in odor localization and tracking, many have modeled animal navigation using tropotaxis [5, 4, 13]. A number of studies use Braitenberg vehicles (robots with simple sensor-motor connections that produce complex behaviors) equipped with bilateral sensors to detect chemicals in the environment, such as gas leaks (reviewed in section 6 of [16]).

In this paper, we present a mathematical analysis of tropotaxis in the presence of smooth odor sources and trails. We provide a fairly comprehensive analysis of the model dynamics, which in several cases reduces to a planar dynamical system. In the first section, we study the dynamics on an infinite trail. We show that there are always two stable fixed points and that there is an optimal sensor angle for attraction to the trail. We also show that the basin of attraction can be estimated from an associated integrable system. We next consider circularly symmetric trails, which include a single spot as well as circular trails. The dynamics is more complicated here and we explore several different regimes including long sensors and sensors that are oriented behind the animal. Finally, we consider more complicated odor landscapes such as partial trails and multiple odor sources. Here we also study trails with gaps and trails that branch and make sharp turns.

2. The Model. The model that we will analyze describes a navigation mechanism in which the angle of the heading (θ) of the individual depends on the difference between the concentration detected by the left and right sensors (see Figure 1). The (X, Y) position of the individual is a function of the heading angle and the individual's speed v, which we will fix to be constant: the individual is always moving. The sensors have length l and are separated by an angle ϕ between them. They are located at the left and the right of the individual's body at positions $(X+l\cos(\theta+\phi), Y+l\sin(\theta+\phi))$ and $(X + l\cos(\theta - \phi), Y + l\sin(\theta - \phi))$ and detect odor concentrations C_L and C_R, where the concentration is generally a smooth gradient in some shape such as a line or a point source. The bilateral olfactory navigation model equations are

$$\dot{X} = v\cos\theta,$$

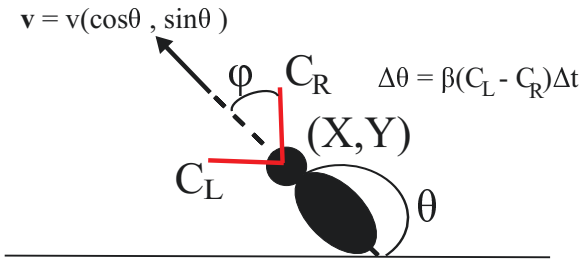

Fig. 1 *The bilateral model: an animal centered at (X, Y), heading in the direction θ. The sensors are length l with angles $\pm\phi$ around the axis of the body. Orientation is governed by the difference in concentrations at the two sensors $C_L - C_R$ and speed is constant v.*

$$\dot{Y} = v \sin\theta,$$
$$\dot{\theta} = \beta\big[C_L(X, Y, \theta) - C_R(X, Y, \theta)\big].$$

The parameter β is the sensitivity to odor differences. If the concentration is greater on the left, the individual turns left, and vice versa. To make the model dimensionless, we propose a change of variables $(X, Y, t) \to (\sigma x, \sigma y, \frac{\sigma}{v}\hat{t})$, where σ is the spread of concentration and v is the velocity. This will change the left sensor position to $(x + \hat{l}\cos(\theta+\phi), y+\hat{l}\sin(\theta+\phi))$, the right sensor position to $(x+\hat{l}\cos(\theta-\phi), y+\hat{l}\sin(\theta-\phi))$, the sensor length to $\hat{l} = \frac{l}{\sigma}$, and the sensitivity to concentration difference to $\hat{\beta} = \frac{\sigma}{v}\beta$. The new model equations are

$$\begin{aligned} \dot{x} &= \frac{\partial x}{\partial \hat{t}} = \cos\theta, \\ \dot{y} &= \frac{\partial y}{\partial \hat{t}} = \sin\theta, \\ \dot{\theta} &= \frac{\partial \theta}{\partial \hat{t}} = \hat{\beta}\big[C_L(x, y, \theta) - C_R(x, y, \theta)\big]. \end{aligned} \tag{2.1}$$

These equations together with the initial conditions give us the bilateral model. We will use this dimensionless model throughout this paper unless otherwise mentioned, and we will drop the $\hat{}$ for easier notation.

3. Infinite Line. We will start by analyzing how the model performs when the odor is along an infinite line. This corresponds to a straight trail along the y-axis. Here, the objective is for the individual to find the trail (i.e., navigate to it) and then keep on it. The odor concentration has a Gaussian profile and is equal to $C(x) = \exp(-x^2)$. (This is the simplification of a point source odor profile; one can use a more principled model based on an advection-diffusion equation (cf. [26, eq. 6, supplement]) but the Gaussian has the advantage of being smooth at the origin, making this analysis possible. Results for other odor profiles are qualitatively similar.) Since the concentration is independent of y, the equations are reduced to a simple planar ODE:

$$\dot{x} = \cos\theta,$$
$$\dot{\theta} = \beta\big[C_L(x, \theta) - C_R(x, \theta)\big].$$

The fixed points of the system are at $(0, \pm\frac{\pi}{2})$ and correspond to finding the trail and going either up $(+\pi/2)$ or down $(-\pi/2)$ the trail. Here, we will limit our domain to

$\theta \in [0, \pi]$, and thus the fixed point is at $(0, \frac{\pi}{2})$. This fixed point is stable as long as $\phi \in (0, \pi/2)$, as is the corresponding fixed point at $-\pi/2$. The trace and determinant of the linearization are, respectively,

$$\begin{aligned} \text{Tr} &= -2\beta l^2 \sin(2\phi) \exp(-(l \sin \phi)^2), \\ \text{Det} &= 4\beta l \sin(\phi) \exp(-(l \sin \phi)^2). \end{aligned}$$

Since the trace is negative and the determinant is positive for all $\phi \in (0, \pi/2)$, the fixed point is asymptotically stable. This fixed point shifts horizontally if the lengths of the sensors are not the same. It becomes a saddle point when the sensors are crossed, in which case the individual will not be able to navigate the odor trail. Also, the individual will not find the trail when one of its sensors is cut. The left panel of Figure 2(A) shows a pair of trajectories, one which misses the equilibrium and travels off to the right and the other which eventually lands on the fixed point, suggesting that there is a basin of attraction for the fixed point. The right panel of Figure 2(A) shows the projection of these trajectories in the (x, y)-plane. Figure 2(B) shows the basin of attraction for $l = 0.2, \phi = 1, \beta = 10, 1$ in solid red and blue, respectively. (These curves are computed by integrating backwards starting at $x = \pm 5$ and with θ close to $\pi/2$.) Any initial data contained within the solid curves will be attracted to the fixed point $(0, +\pi/2)$ and any initial data outside this region will go off to $\pm\infty$. As is expected, the blue region lies entirely in the red region. Intuitively, if the individual is too far away from the source, unless it is nearly aligned with the trail, the concentration difference will never become large enough to allow it to correct. We can put this intuition on a more rigorous footing by assuming the sensor length l is small, to get (via Taylor's theorem)

$$C_L - C_R = [4l \sin \phi]\, x \exp(-x^2) \sin \theta + O(l^2),$$

so that we obtain the approximate system

$$\begin{aligned} \dot{x} &= \cos \theta, \\ \dot{\theta} &= [\beta l \sin \phi]\, x \exp(-x^2) \sin \theta. \end{aligned}$$

This ODE is integrable, with

$$E(x, \theta) := -2\beta l \sin \phi \exp(-x^2) - \log(|\sin \theta|) = \text{constant}.$$

$E(x, \theta) = 0$ corresponds to a pair of trajectories (shown by the dashed lines in Figure 2(B)) that separate bounded ($E < 0$) from unbounded ($E > 0$) trajectories. As can be seen in the figure, these curves are reasonable approximations to the full basin of attraction (at least for l small).

3.1. Sensor Angles. The sensor angles play an important role in the ability to find and follow a trail. Furthermore, they are something that can be under the control of the animal, whereas sensitivity and sensor length would be difficult to vary. Figure 3(A) shows the basin of attraction for a trail with $\beta = 10, l = 1$ as ϕ is varied from the nominal value $\phi = 1$ to $\phi = 0.2, 1.5$ and $\phi = 0.57$ (the angle at which the trace is minimum for $l = 1$). Consider the upper part of the diagram (the bottom is similar under the transformation $x \to -x, \theta \to \pi - \theta$). As ϕ increases toward $\pi/2$ (blue curve) and $x(0) > 0$, the individual must be more closely aligned with the trail ($\theta(0)$ closer to $\pi/2$). For $x(0) < 0$, the initial heading does not matter as long

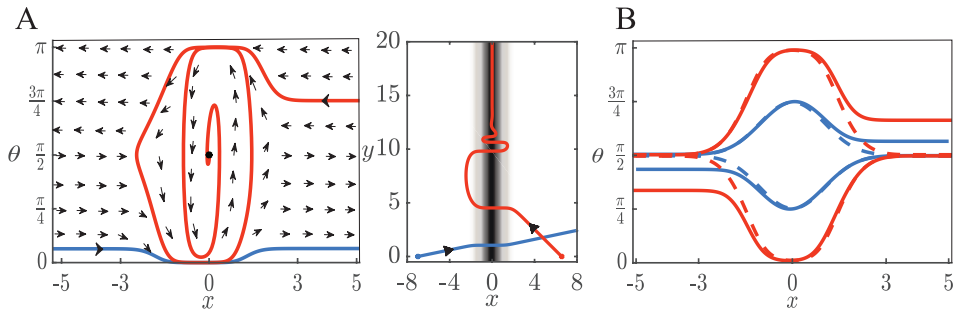

Fig. 2 (A) *(left) Phase plane when the trail is an infinite line. One trajectory converges to the stable fixed point at* $(0, \frac{\pi}{2})$ *but the other does not. From the vector field, a separatrix can be observed around the line* $\theta = \pi/2$. *(right) Projection of the solutions in the* (x, y)*-plane.* (B) *Basin of attraction of the trail. The dashed lines are the separatrices for the integrable system that separate the bounded solutions from the unbounded solutions. The solid lines are the numerically simulated basins. The blue lines represent the basin when* $\beta = 1$ *and the red lines the basin when* $\beta = 10$. *Here,* $\phi = 1, l = 0.2$.

as $x(0)$ is close enough to the trail and, in this case, there is a slight advantage to increasing the angle. On the other hand, with small ϕ (black curve), there seems to be no difference from $\phi = 1$ for $x > 0$, but for $x < 0$ the basin is decreased. While we have not measured the precise area of the basin, it would appear that $\phi = 1$ (green) has the largest area, losing a little for $x < 0$ but keeping the maximal amount for $x > 0$. We also note that when $\phi = 0.57$ (red), the basin is very close to that of $\phi = 1$.

The basin is impossible to compute analytically, but a plausible surrogate is the divergence of the vector field at the fixed point $(x, \theta) = (0, \pi/2)$. We thus consider the trace of the linearization around the fixed point given above. We plot this quantity as a function of ϕ for several different values of l as shown in Figure 3(B). Clearly, as l increases the minimum shifts toward lower values of ϕ. With a little bit of calculus and algebra, we find that

$$\cos \phi_{min} = \sqrt{\frac{l^2 + \sqrt{l^4 + 1} - 1}{2l^2}}.$$

The right-hand side ranges between $1/\sqrt{2}$ and 1 as l ranges between 0 and ∞. This suggests that the sensors should have an angle between them that is between 0 and $\pi/2$. The distance between the sensors is $2l \sin \phi$, yielding the optimal distance as

$$d_{opt}(l) = \sqrt{2\, l^2 - 2\, \sqrt{l^4 + 1} + 2}.$$

d_{opt} saturates near $l = 2$ at $\sqrt{2}$, which suggests that the optimal sensor distance for staying on a trail whose characteristic width is σ will be $\sqrt{2}\sigma$.

To summarize, a single infinite odor trail greatly simplifies the dynamics to a planar system. There are only two fixed points, both always stable, corresponding to moving up or down the trail. There is an optimal angle for the sensors that maximizes the stability and decreases with the sensor length. The basin of attraction is well approximated by a simple analytic formula for an associated integrable system.

4. Radially Symmetric Landscapes. We now turn our attention to odor landscapes that are radially symmetric, which include point sources and circular trails.

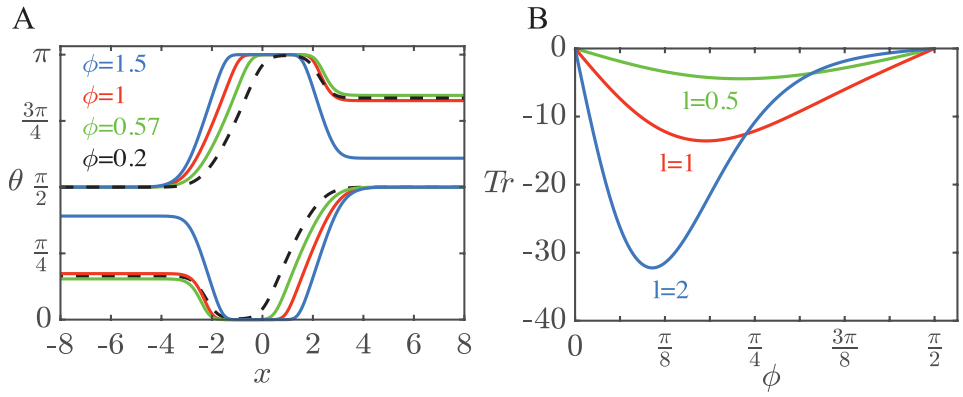

Fig. 3 (A) *Basin of attraction for the stable fixed point* $(0, \pi/2)$ *for trail following as a function of initial orientation and* x*-position for* 4 *different sensor angles,* ϕ*. Remaining parameters are* $l = 1, \beta = 10$*.* (B) *Trace of the linearization about the stable fixed point as the angle between the sensors varies.*

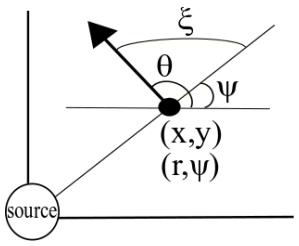

Fig. 4 *Change of variables when odor landscape is radially symmetric.* (r, ψ) *are the polar coordinates introduced when the individual is at position* (x, y) *and has a heading angle* θ*.* ξ *is the relative coordinate* $\xi = \theta - \psi$*.*

This symmetry allows us to again reduce the three-dimensional dynamical system to a planar system. We introduce polar coordinates r, ψ $(x = r\cos\psi, y = r\sin\psi)$ and the relative coordinate $\xi = \theta - \psi$. Note that $\xi = 0$ (resp., $\xi = \pi$) corresponds to heading away from (resp., toward) the source along a radial line (see Figure 4). With these coordinates, we again obtain a planar system:

$$\begin{aligned} \dot{r} &= \cos\xi, \\ \dot{\xi} &= \beta\big[C_L(r,\xi) - C_R(r,\xi)\big] - \frac{1}{r}\sin\xi := G(r,\xi). \end{aligned} \tag{4.1}$$

With a radially symmetric concentration $C(r)$, the left and right concentrations are

$$\begin{aligned} C_L(r,\xi) &= C\big(\sqrt{r^2 + l^2 + 2lr\cos(\xi + \phi)}\big), \\ C_R(r,\xi) &= C\big(\sqrt{r^2 + l^2 + 2lr\cos(\xi - \phi)}\big). \end{aligned}$$

Any equilibria will have $\xi = \pm\pi/2$ and $r = \bar{r}$ chosen to solve $G(\bar{r}, \pm\pi/2) = 0$. These fixed points correspond to the individual moving counterclockwise (resp., clockwise) around the source at a constant velocity. Whether such fixed points exist and whether they are stable is the subject of the rest of this section.

In what follows, we will assume the concentration has the form $C(r) = \exp(-(r - r_0)^2)$, where the peak concentration forms a ring of radius r_0 around a central point.

Note that $r_0 = 0$ is a point source. As noted above, there are two different values of ξ corresponding to equilibria; since they just represent the individual going clockwise or counterclockwise, we will focus on the $\bar{\xi} = \pi/2$.

Remark 4.1. We have chosen a simplistic model for the circular trail, $C(r, r_0) = \exp(-(r - r_0)^2)$, which is not a physical possibility. Rather, the correct form is to convolve the Gaussian with a Dirac distribution on a circle. The result is

$$C_{real}(r, r_0) = N(r_0) I_0(2r_0 r) \exp(-2r_0 r) \exp(-(r - r_0)^2),$$

where I_0 is the modified Bessel function of the first kind and $N(r_0)$ is chosen so that $C_{real}(r, r_0)$ has a maximum value of 1. One problem is the computation of $N(r_0)$, since there is no simple analytical expression for the value of r maximizing C_{real}. For r_0 close to zero, the two forms are indistinguishable, and for $r_0 > 2$, they are also quite close. Thus, it is only for values of r_0 around 1 that there are differences. (Recall that we have scaled the width of the Gaussian to be 1.) We have reproduced all the phase portraits except those in Figure 6 using the physically correct concentration. However, we also note that we have only approximated $N(r_0)$, since no analytic expression exists and the behavior in Figure 6 occurs for a very limited range of r_0.

Figure 5(A) shows the behavior of the model when $r_0 = 0$, a point source. The top figure shows the phase plane for (4.1). There are two fixed points: the one closest to $r = 0$ is an unstable source, and the larger one is a saddle point. The stable (cyan) and unstable (orange) manifolds are drawn. While there are no attractors in this case, the stable manifolds still play an important role in the dynamics. If the initial data lies above them, then solutions in the (x, y, θ) system will pass through the odor spot, as seen in the (x, y)-projection in the bottom of the panel. Initial data below the manifolds will veer off without getting closer to the spot. While there are no attractors (there is no "trail" to follow), from a practical point of view, any initial condition above the stable manifolds will "find" the spot. The bifurcation diagram in Figure 5(D) shows the behavior of the small r fixed point as r_0 increases. At $r_0 \approx 0.5$, the unstable source becomes a stable sink via a Hopf bifurcation. A branch of unstable periodic orbits (blue curves) emerges and terminates at an orbit homoclinic with the saddle point (not shown). We remark that for large r_0, the stable equilibrium is $r \approx r_0$, so the individual is centered on the trail just as in the line trail. Figure 5(C) top (bottom) panel shows the (r, ξ) phase plane ((x, y)-projection) for $r_0 = 4$. In this case, the stable manifolds form the basin of attraction for the circular trail. Any initial condition starting within the basin will find and follow the trail (blue trajectories), while any initial condition outside the basin will not follow it (red trajectories). Figure 5(B) shows the (r, ξ) phase plane for $r_0 = 1$. In this case, the basin is the unstable periodic orbit that is the α-limit set of one of the branches of the stable manifold. If one of the sensors is cut, the individual converges to a new stable periodic orbit (in the (x, y)-plane) with a smaller radius, as long as it starts in the region bounded by the circular trail.

4.1. Dependence on the Model Parameters. The stabilization of the fixed point as r_0 increases occurs via a Hopf bifurcation. In what follows, we explore this dependence in detail.

4.1.1. Sensor Angle. The sensor angle ϕ provides an interesting picture. We first note that if we let $\hat{\phi} = \pi - \phi$ and $\hat{\xi} = \xi + \pi$, then (4.1) becomes

$$\frac{dr}{dt} = -\cos\hat{\xi},$$

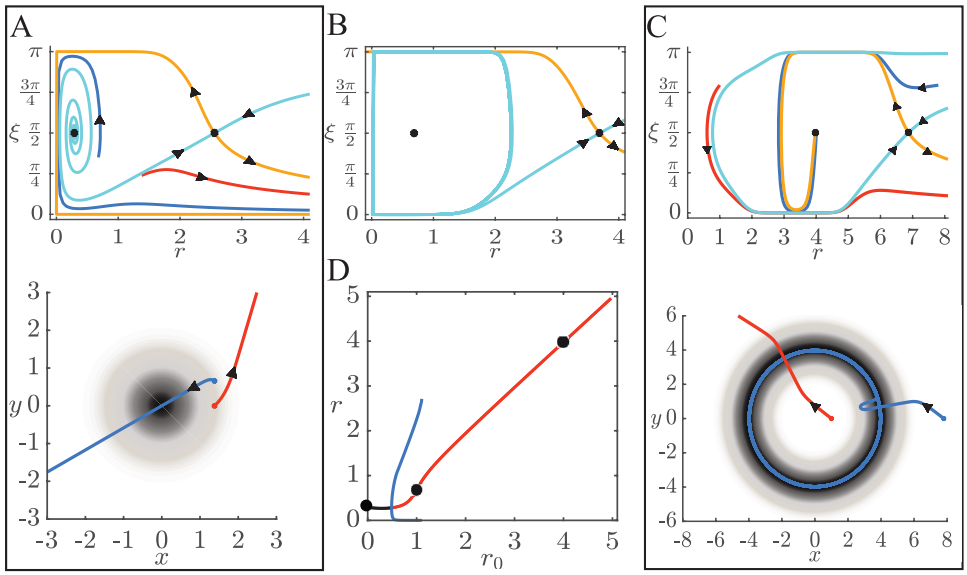

Fig. 5 (A) *(top) Phase plane for* (4.1) *for* $r_0 = 0$*, a spot source showing an unstable spiral (near* $r = 0.4$*) and a saddle (near* $r = 2.5$*) along with its stable (cyan) and unstable (orange) manifolds and two trajectories. (bottom) Projection of the solutions in the* (x, y)*-plane.* (B) *Phase plane for* $r_0 = 1$*. The stable manifold forms an unstable limit cycle. As shown in the bifurcation diagram* (D)*, the fixed point inside is stable. The fixed point inside is stable.* (C) *(top) Phase plane for* $r_0 = 4$ *with the same conventions as in panel* (A)*. Note that the unstable spiral has become an attractor. (bottom) Projection in the* (x, y)*-plane.* (D) *Bifurcation diagram as a function of the trail radius* r_0*; stable (unstable) fixed points are red (black) and unstable limit cycles are blue. Black dots correspond to* $r_0 = 0, 1, 4$ *and the phase planes in* (A), (B), (C)*. Parameters are* $\beta = 10, \phi = 1, l = 1$*.*

$$\frac{d\hat{\xi}}{dt} = -\left(\beta\left[C_L(r,\hat{\xi}) - C_R(r,\hat{\xi})\right] - \sin\hat{\xi}/r\right),$$

with $\hat{\phi}$ replacing ϕ. Angles $\phi \in (\pi/2, \pi)$ correspond to the individual having its sensors behind it. This calculation shows that the vector field for $\phi \in (\pi/2, \pi)$ is the same as that for $\phi \in (0, \pi/2)$ in reverse time. Thus, for example, unstable periodic orbits for $\phi \in (0, \pi/2)$ become stable periodic orbits for $\phi \in (\pi/2, \pi)$. In addition, note that if $\phi = \pi/2$, then (4.1) is a reversible system, since $\xi \to \xi + \pi$ takes $t \to -t$. Thus, for fixed r_0 and increasing ϕ from 0, there will be three Hopf bifurcations; the middle one is degenerate and located at $\phi = \pi/2$, the reversible system. To gain more insight into the full dynamics, we look at the (ϕ, r_0) parameter plane in more detail. Figure 6 shows bifurcation diagrams as ϕ varies for several different values of r_0. There are several notable features. The central diagram shows the curves of Hopf bifurcations (blue) in addition to curves of saddle-nodes of limit cycles (SNLCs, black). The latter curve is nonmonotonic, so that there is a region (below the red dashed curve) where there can be two SNLCs. The lower right diagram shows that these delineate an isola (isolated branch) of periodic orbits. As r_0 increases, this isola merges with the branch of unstable periodic orbits (lower left diagram). Between $r_0 = 0.51$ and $r_0 = 0.55$, the stable and unstable branches collide with the saddle at a saddle-homoclinic bifurcation (shown as H in the upper right diagram). Finally, the SNLC merges with the Hopf bifurcation curves (shown by the asterisk in the central figure), leaving an unstable

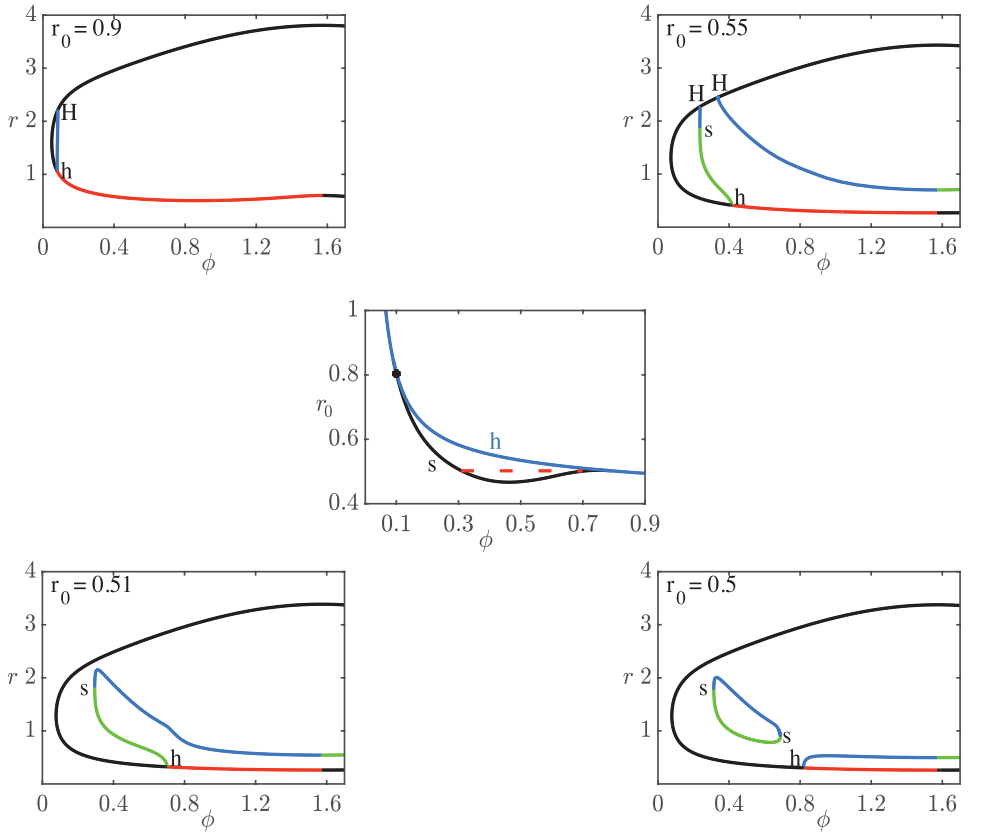

Fig. 6 *Behavior as r_0, ϕ vary. The center figure shows the two-parameter (ϕ, r_0)-plane. The blue line denotes the curve of Hopf bifurcations. Above this curve there is a stable fixed point. The black line is the curve of saddle-node bifurcations of periodic orbits. Below the red dashed line there are two SNLCs (isola). One-parameter bifurcation diagrams are shown for different values of r_0 as ϕ varies. Black (red): unstable (stable) fixed points; blue (green): unstable (stable) periodic orbits. (h): Hopf bifurcations; (s): SNLCs; (H): saddle-homoclinic orbits.*

periodic orbit (upper left diagram; the other unstable periodic orbit is not shown). The apparent existence of stable periodic orbits for small radius trails and small sensor angles implies that there is a stable torus in the full (x, y, θ) system.

4.1.2. Sensor Length. Surprisingly, we have found multistability on circular trails of radius r_0 for sensors that have the same approximate length $l \approx r_0$ and small attraction β. Figure 7 shows some examples of the dynamics. Here, we choose $r_0 = 4$ and l between 4 and 6, while letting β range between 0.5 and 3.5. The dynamics is organized around the two-parameter curves of various bifurcations (not all of them are shown, either for clarity or due to an inability to follow them). In the figure, curves of saddle-node bifurcations of equilibria (SNE) are shown in red, Hopf bifurcations in blue, and a homoclinic bifurcation in olive. Phase planes in some of the regions are shown. We emphasize once again that stable fixed points (limit cycles) in this reduced system correspond to stable periodic orbits (tori) in the full three-dimensional model (see Figure 8). Starting in region a, there is a single attracting

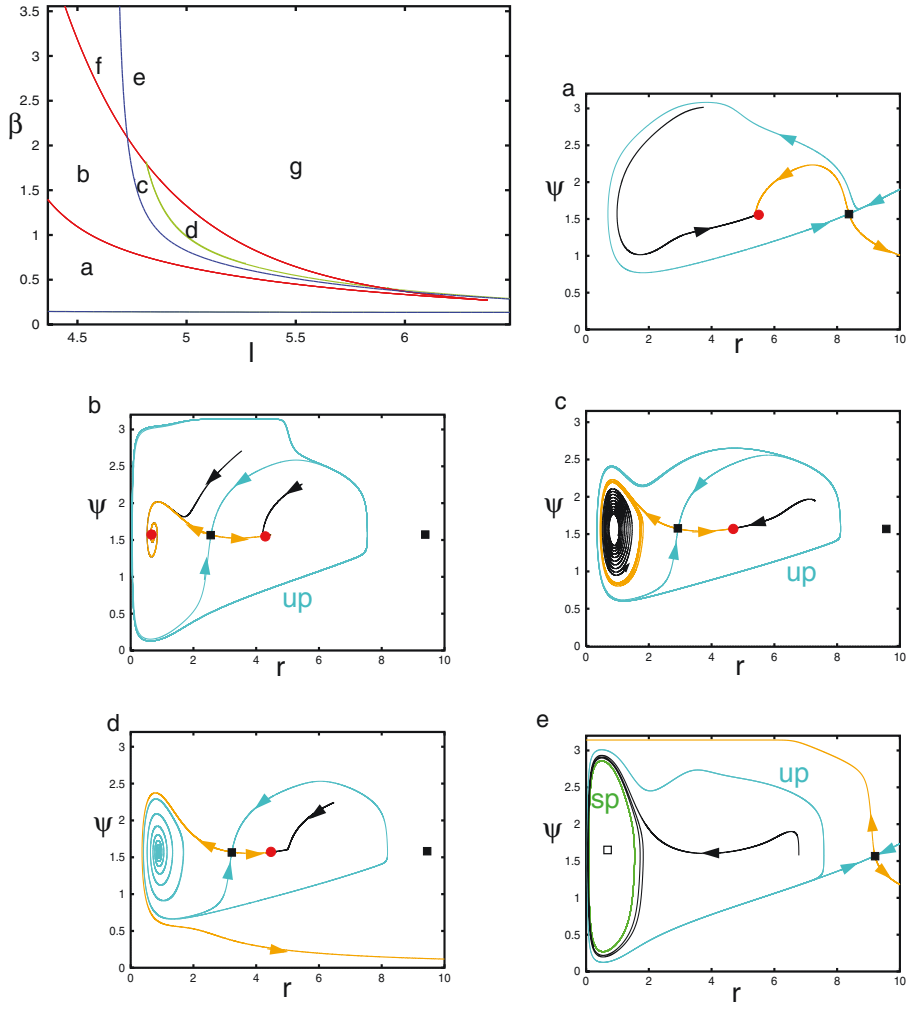

Fig. 7 *Dynamics on a circular trail (here $r_0 = 4, \phi = 1$) when l is large and β is small. The dynamics is organized by the saddle-nodes or folds of equilibria (red), the Hopf bifurcation (blue), and a homoclinic bifurcation (olive). Phase planes in the representative regions are depicted. Stable (cyan) and unstable (orange) manifolds of the saddles (filled black squares) are shown along with some representative trajectories (black). Stable fixed points are red circles, saddles are black squares, unstable nodes are hollow squares. UP: unstable periodic orbit; SP: stable periodic orbit. Region f is like region e, but the stable periodic orbit is replaced by a stable fixed point. In region g, there are no attractors. Panel* (e) *shows a stable isolated limit cycle in green. More details are given in the text. Parameters (l, β):* (a) $(4.5, 0.5)$, (b) $(4.5, 2)$, (c) $(4.85, 1.25)$, (d) $(4.93, 1.25)$, (e) $(4.72, 3)$.

fixed point whose basin is delineated by the stable manifolds of the outer saddle. (As we will eventually encounter another saddle point, the outer one will be the one that is at roughly $r = 9$. It persists throughout the figure.) Two bifurcations occur as we move from a to b. First, there is a homoclinic bifurcation at the outer saddle leading to an unstable periodic orbit (UP) that plays the role of the basin for the fixed point. (This is not shown as a separate phase plane since the attractor structure is still the

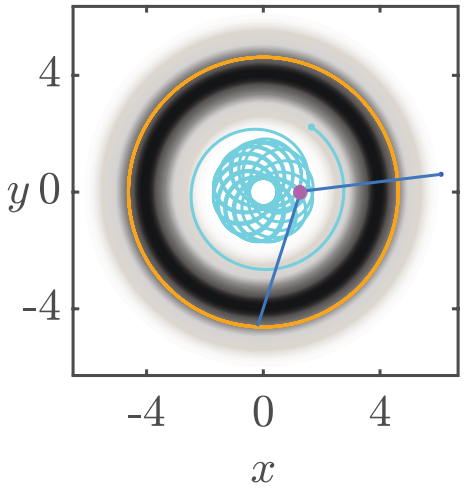

Fig. 8 *Projection of the trajectory of the individual in the (x, y, θ) model in region* c *of Figure* 7. *The outer orange circle is a stable path of the individual, and the grayscale shows the trail concentration. The stable torus solution is shown in cyan. The magenta spot is the individual with the sensors drawn to scale in blue. The animation can be found in the supplementary video.*

same.) As we cross the red curve into region b, two new fixed points arise: a stable node and a saddle. The UP continues to provide the basin, but the stable manifolds of the inner saddle (near $r = 2$) split this basin between the two stable fixed points. Recalling that $r_0 = 4$, we see that the outer fixed point shows the individual following the trail, while with the inner stable fixed point the individual makes smaller circles within the trail. In the transition from b to c, the inner fixed point undergoes a Hopf bifurcation and spawns a stable periodic orbit (SP). Thus, in the (x, y, θ) model there is bistability between the individual tracking the trail and a quasi-periodic trajectory that lies near the center of the trail. Figure 8 shows the dynamics in the (x, y)-plane. The transition from c to d occurs through a homoclinic bifurcation (olive curve) where the SP disappears. The result is just a single attractor. In d to g, this attractor is lost via an SNE and there remain no attractors. The path from c to e occurs via an SNE leaving just an SP whose basin is determined by the UP. The transition from e to g occurs when the SP and the UP (SNLC) merge and disappear. The transition from e to f occurs when the limit cycle disappears through a reverse Hopf bifurcation stabilizing the fixed point shown by the hollow square. Region f has only one attractor; this stabilized fixed point is near $r = 1$ and is not shown. We were unable to compute the curve of SNLCs delineating the transition from e to g.

4.1.3. Basins of Attraction. Given a circular trail sufficiently large that there is a stable fixed point, we first examine the dependence of the basin on the radius and the turning sensitivity β in Figure 9. In Figure 9(A), $r_0 = 1$ and $\beta = 1, 10$, while in Figure 9(B), $r_0 = 4$. For smaller radii, higher sensitivity does not necessarily mean that the basin will be bigger. Indeed, there are initial conditions that lie in the basin of attraction for $\beta = 1$ (red), but not when $\beta = 10$ (blue). On the other hand, for large radii (see Figure 9(B)), the basin for $\beta = 10$ contains the basin for $\beta = 1$.

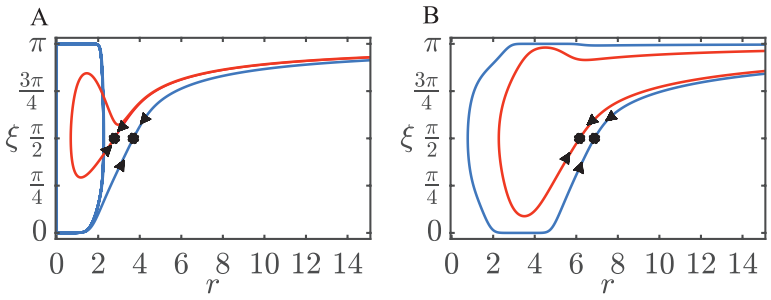

Fig. 9 (A) *Basin of attraction when the trail is circular with radius* $r_0 = 1$. (B) *Basin of attraction when the trail is circular with radius* $r_0 = 4$. *For both figures, blue and red lines correspond to the basin when* $\beta = 10$ *and* $\beta = 1$, *respectively.*

Since there are no stable fixed points for spot location, we can consider the ability of an individual to orient toward a spot given that it is frozen ($v = 0$) at a distance r from the spot. In this case, we have a simple one-dimensional system

$$\dot{\xi} = \beta\big[C_L(r,\xi) - C_R(r,\xi)\big]$$

with a stable fixed point at $\xi = \pi$. The eigenvalue around this fixed point is

$$\lambda(r,l,\phi) = -\beta 4lr\sin(\phi)\exp(-r^2 - l^2 + 2lr\cos(\phi))$$

and, as with the trail, this has a minimum at a particular value of ϕ:

$$\cos\phi = \frac{-1+\sqrt{16(rl)^2+1}}{4rl} := M.$$

As $rl \to 0$, $M \to 0$ and as $rl \to \infty$, $M \to 1$. In particular, this suggests that close to the spot (rl small), the animal should keep its sensors near $\pm\pi/2$, while it should keep them close to 0 when it is far from the spot.

4.1.4. Integrability. As in the case of an infinite line, system (4.1) can be approximated by an integrable system for small l:

$$\begin{aligned} \dot{r} &= \cos\xi, \\ \dot{\xi} &= [4l\beta\sin(\phi)(r-r_0)\exp(-(r-r_0)^2) - 1/r]\sin\xi, \end{aligned} \tag{4.2}$$

with

$$E := log(|\sin\xi|) + 2l\beta\sin(\phi)\exp(-(r-r_0)^2) + log(r) = \text{constant}.$$

For $K := \beta l\sin(\phi)$ large enough, the integrable system has a saddle and a nonlinear center; the stable manifolds of the saddle form a good approximation for the basin of attraction for (4.1), even for $l = 1$, over a wide range of the other parameters. This calculation does not say anything about the stability of the fixed point; rather, it gives some insight into the regions of attraction. Figure 10 shows that even for $l = 1$, the basins of the full equation (4.1) and the integrable system (4.2) are close.

As with the linear trail, radially symmetric odor gradients can also be reduced to planar dynamical systems. Nevertheless, they produce complex behaviors including multistability and different types of stable and unstable limit cycles. Circular trails

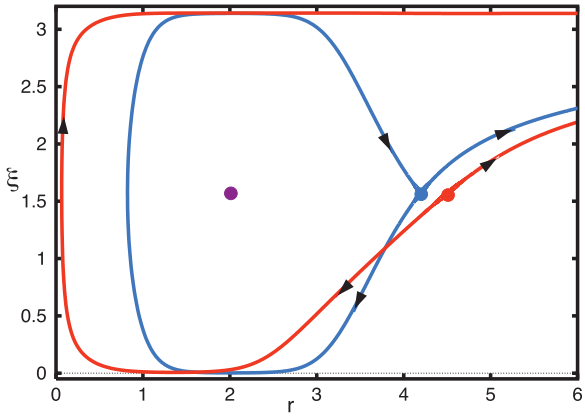

Fig. 10 *Comparison of the basin of attraction for the full model* (4.1) *(red) with that of the integrable approximation* (4.2) *(blue) for* $l = 1, \beta = 4, r_0 = 2, \phi = 1$. *Saddle points are shown in their respective colors. The stable fixed point and nonlinear center are nearly coincident and are shown in purple.*

with a large enough radius lead to a stable movement clockwise or counterclockwise around the trail when the sensors are short. Such trajectories are seen in so-called ant mills (where large populations of ants move in a circular trail until they die of exhaustion) [25]. Because the individual has a constant speed, it is not possible for the point source to be an attractor. However, the model does take the individual toward the source (depending on its initial distance and heading), so, in a real situation where the source is some reward, the animal would stop moving when it reached the source.

5. Multiple Sources. When an animal is searching for food, there can be multiple sources that affect the concentration detected and could be used to localize an odor source. We next study how the bilateral model behaves in the presence of two odor sources. With more than one source, the radial symmetry is broken and we cannot exploit the reduction in dimension used above. Thus, we will use the (x, y, θ) system and the concentration detected will be the sum of the Gaussian concentrations of the spots.

Without loss of generality, we place the *two* point sources at a distance d from each other on the x-axis and analyze the dynamics of (2.1). The odor concentration at the first spot is $C_1(x, y) = A_1 \exp(-((x + d/2)^2 + y^2))$, and at the second spot is $C_2(x, y) = A_2 \exp(-((x - d/2)^2 + y^2))$, where A_1 and A_2 are positive, possibly different, amplitudes. Thus, the concentration detected at the sensors is

$$C_L(x, y) = C_1(x_L, y_L) + C_2(x_L, y_L),$$
$$C_R(x, y) = C_1(x_R, y_R) + C_2(x_R, y_R),$$

where $x_{L,R}, y_{L,R}$ are as in Figure 1.

Recall that in the case of a *circular trail*, there are stable fixed points in the polar form of the equations which correspond to circular periodic orbits in the (x, y, θ) system. Since the individual must maintain a constant speed, we cannot expect any fixed points in the (x, y, θ) system, so we will look for periodic orbits. We fix $\beta = 20, l = 0.5, \phi = 1$ in this section; the default values of β, l produce periodic orbits for a range of d, but the behavior is not as rich. In Figure 11(A), we show two

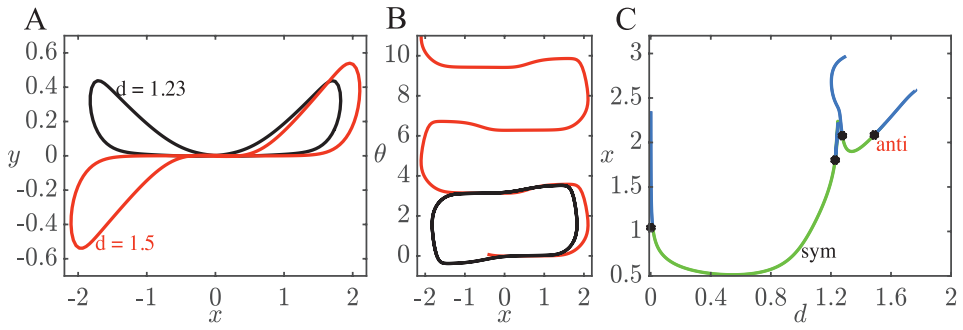

Fig. 11 *Two different types of trajectories for concentrations with two odor sources located on the x-axis a distance d apart, centered at x = 0.* (A) *Projection in the (x, y)-plane.* (B) *Projection in the (x, θ)-plane.* (C) *Bifurcation diagram for the two different cases in* (A) *and* (B) *as d varies. Other parameters are β = 20, l = 0.5, φ = 1.*

qualitatively different trajectories projected in the (x, y)-plane for spots placed at a distance d on the x-axis. At small values of d, the trajectory is symmetric (black curve) and the heading θ oscillates around $\pi/2$ (Figure 11(B), black) (topological winding number of 0). There is an analogous curve where $y(t) < 0$ and θ oscillates about $3\pi/2$. For a larger value of d, we find an antisymmetric trajectory (Figure 11(A), red) and in this case, θ goes through all values with a net increase of 2π after each cycle (Figure 11(B), red) (topological winding number of 1). Figure 11(C) shows the one-parameter bifurcation diagram as d changes for the symmetric and the antisymmetric paths. The stability of these is lost at branch points marked by the filled blue circles. If we follow the symmetric branch point at the high value of d (close to 1.25), then a stable branch of asymmetric solutions emerges. This is shown in Figure 12(A) as the blue curve. Increasing d along this asymmetric branch leads to a periodic doubling bifurcation (shown as the black curve). Further increases lead to presumably chaotic behavior, shown in Figure 12(B) in the (x, y)-plane. To further quantify the chaos, we take a Poincare section through $x = 1.75$ and plot the points (y_n, θ_n), where x crosses from right to left. We find (not shown) that these points appear to lie along a one-dimensional curve, indicating that the underlying chaos can be understood by a one-dimensional map. Figure 12(C) shows the map where we plot (y_n, y_{n+1}). It appears to be a typical cap map. The periodic orbit (blue circle) is unstable as the slope through it is less than -1. Figure 12(D) shows (y_n, y_{n+3}) plotted and a clear period-3 orbit that is also unstable. Since the underlying dynamics seems to be governed by a one-dimensional map, we believe that Figure 12(B) represents a truly chaotic orbit. Additionally, the maximal Liapunov exponent is 0.045, a positive number, yet another characteristic of chaos.

As the previous figures show, if the spots are close to each other, there can exist solutions where the individual circles *both of them*. Furthermore, when there is an isolated spot, there are no stable bounded solutions, as we saw above. However, the presence of a distant spot (at least over a small range of distances) can stabilize periodic orbits around a spot. Figure 13(A) shows two different stable trajectories around a source at $(-d/2, 0)$. The red solution is symmetric about the y-axis ($d = 2.5$) and the black solution has lost the symmetry ($d = 2.43$). This branch of periodic solutions exists for a narrow range of values of d, as shown in the bifurcation diagram in Figure 13(B). In particular, as d decreases, there is a supercritical pitchfork bifurcation that leads to the stable asymmetric solution shown in panel (A). For d increasing, there

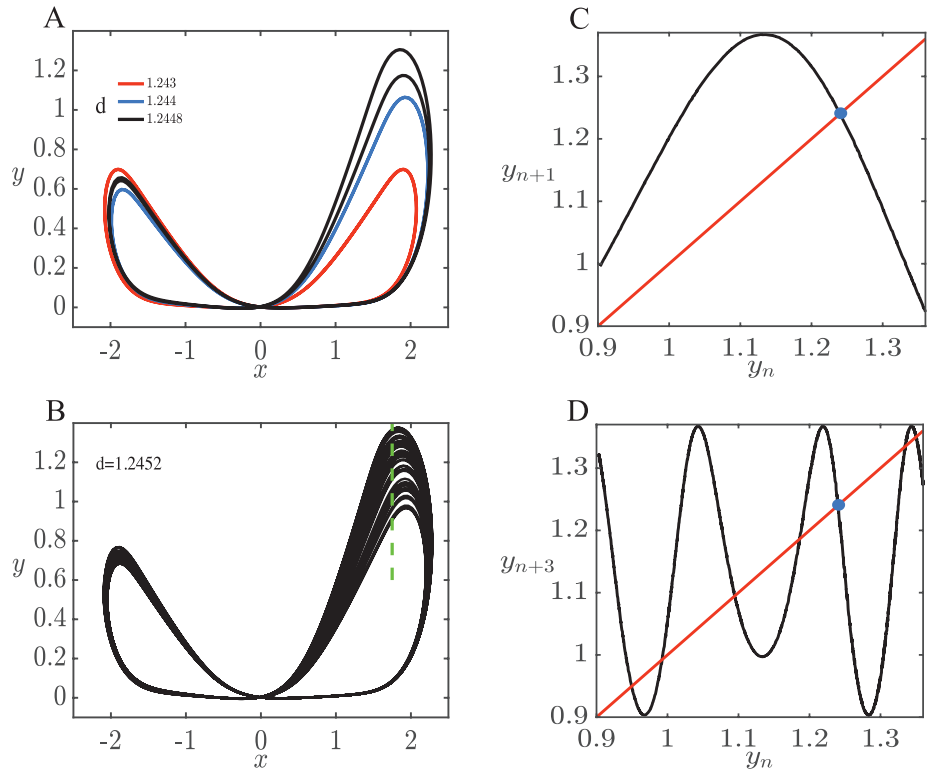

Fig. 12 *Behavior of* (2.1) *when there are two Gaussian sources at* $(x, y) = (\pm d/2, 0)$. (A) *As* d *increases, the symmetric periodic solution (red) loses stability and gives rise to a stable asymmetric solution (blue). Increasing* d *leads to a period doubled solution (black) which also loses stability as* d *increases.* (B) *Presumably chaotic behavior for* $d = 1.2452$. (C) *Poincaré map through* $x = 1.75$ *for the solution in* (B). *The blue circle is the unstable periodic orbit.* (D) *Same Poincaré section showing the numerical existence of a period-3 orbit shown by the intersections of the* $n+3$ *iterate with the diagonal. The blue filled circle shows the period-1 fixed point. (Parameters are as in Figure* 11.*)*

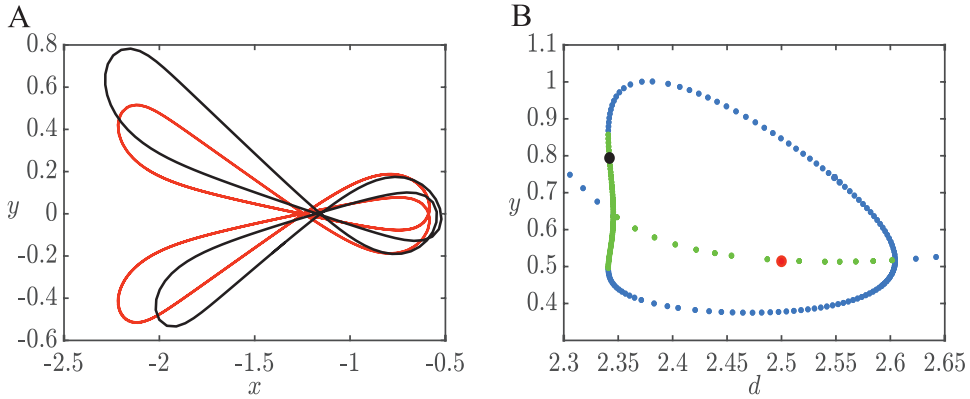

Fig. 13 *Two distant sources.* (A) *Stable periodic circling around the source at* $(-d/2, 0)$ *with the other source located at* $(d/2, 0)$ *with* $d = 2.5$ *(red) and* $d = 2.34$ *(black).* (B) *Bifurcation of the isolated periodic orbit as* d *changes. There are two pitchfork bifurcations whose branches form an isolated loop. Filled circles correspond to orbits depicted in A. Remaining parameters are as in Figure* 11.

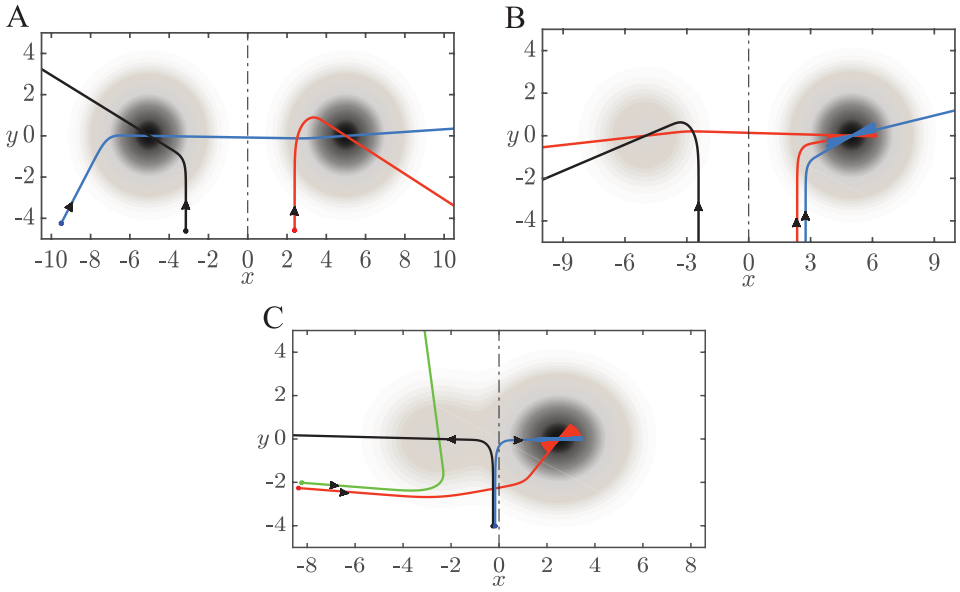

Fig. 14 *Different trajectories when* (A) *both sources have the same amplitude* ($A_1 = A_2 = 1$) *and are at a distance* ($d = 10$) *where the* 2 *sources are distinguishable;* (B) *the second source has significantly larger amplitude* ($A_2 = 5$)*;* (C) *the second source has significantly larger amplitude and the sources are closer to each other* ($d = 5$)*. Other parameters are as in Figure* 11.

is a subcritical pitchfork which together with the other pitchfork forms an isolated branch of asymmetric solutions.

Another interesting question is how the behavior changes when the concentrations at the spots are different in magnitude. Figure 14(A) shows trajectories when the amplitudes of the spots are equal and the spots are at a relatively large distance from each other (such that there is no periodic orbit encircling them). Depending on the initial position, trajectories either pass through both spots, or just one of the spots, or miss them both. In all cases, however, the trajectories diverge. This is also true when we increase the amplitude of one of the spots by fivefold as in Figure 14(B). Note that the individual spends some time wandering around the spot with higher intensity before wandering off. On the other hand, when we bring the spots closer to each other as well as increase the amplitude (Figure 14(C)), the trajectories that go to the spot with larger amplitude will oscillate around this spot. Thus, the existence of the weaker spot at a distance can stabilize the trajectory around the spot with a higher concentration, just as we saw in Figure 13. The periodic solution shown in Figure 14(C) persists for much larger values of A_2 and will also persist for A_2 reduced to 1, where the resulting periodic solution is the same as that seen in Figure 13(A) (red).

More complex dynamics can occur with three or more sources. In this case, however, there are many different possible configurations, and so we will not consider them further.

6. Finite Trails. We have looked at how the bilateral model performs when we have an infinite line and circular trails. Now we will examine its behavior on a finite

line segment and a finite line segment with gaps, sharp angles, and branches, as these cases can be tested in animal behavior experiments.

If we start close enough to a segment trail, the model will find the trail, follow it, and then leave it. When β or l is small, trajectories will have damped oscillations that decay slower as we decrease β or l (see Figure 15). The starting angle affects the trajectory orientation; most trajectories continue to the right when θ_0 is less than $\frac{\pi}{2}$ and to the left when θ_0 is larger than $\frac{\pi}{2}$. Similarly, if we start around the gap, then we take either the left or right branch depending on the starting position and angle. Also, we can find the trail from significantly farther distances when we start around the gap, which is also the case when we start around the beginning or end of the trail. An individual will cross the gap and reacquire the trail when the gap is in a line trail that has no angles or turns. This is true because once the trail is acquired in the bilateral model, the individual will keep moving straight on it. However, if either β or l is small and the oscillations are large near the gap, the model will sometimes lose the trail as in Figure 15(B).

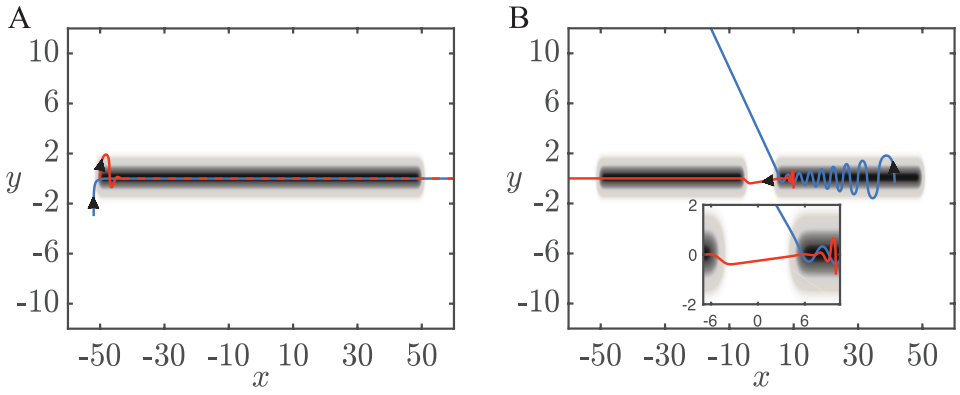

Fig. 15 (A) *Trajectories on a segment trail. The red line is when β is fivefold smaller than the blue line trajectory.* (B) *Trajectories can either cross gaps or lose the trail depending on β or length of nares l. The red trajectory is when $l = 0.4$ and the blue trajectory is when $l = 0.1$.*

If there is an angle in the trail, then it must be larger than $\frac{\pi}{4}$ for the model to follow it easily. In Figure 16(A), the model is able to correct and follow the trail when the angle is slightly bigger than $\frac{\pi}{4}$, but as soon as the corner angle is $\frac{\pi}{4}$, the model loses the trail.

When the trail bifurcates into two branches, the angle and amplitude of each branch determine the trajectories of the model as it passes the branch. We observe that when an individual starts on the main trail that has two branches at equal angle and amplitude (top panel of Figure 16(B)), it will continue on a straight path as there is no difference in the left and right concentrations due to symmetry. However, if the symmetry is broken, say, the branch angles are unequal (bottom panel of Figure 16(B)), then the individual will go toward the branch that requires the least amount of turning. This might not be the case if the concentrations on the two branches differ, as the model will always turn toward the higher of the two concentrations at the sensors.

Trails with gaps and finite trails are similar to an infinite trail over the period of time in which the individual is on the segment, since once the individual finds the trail, it stays on it. If the trail is short and σ is large, then there is behavior like two

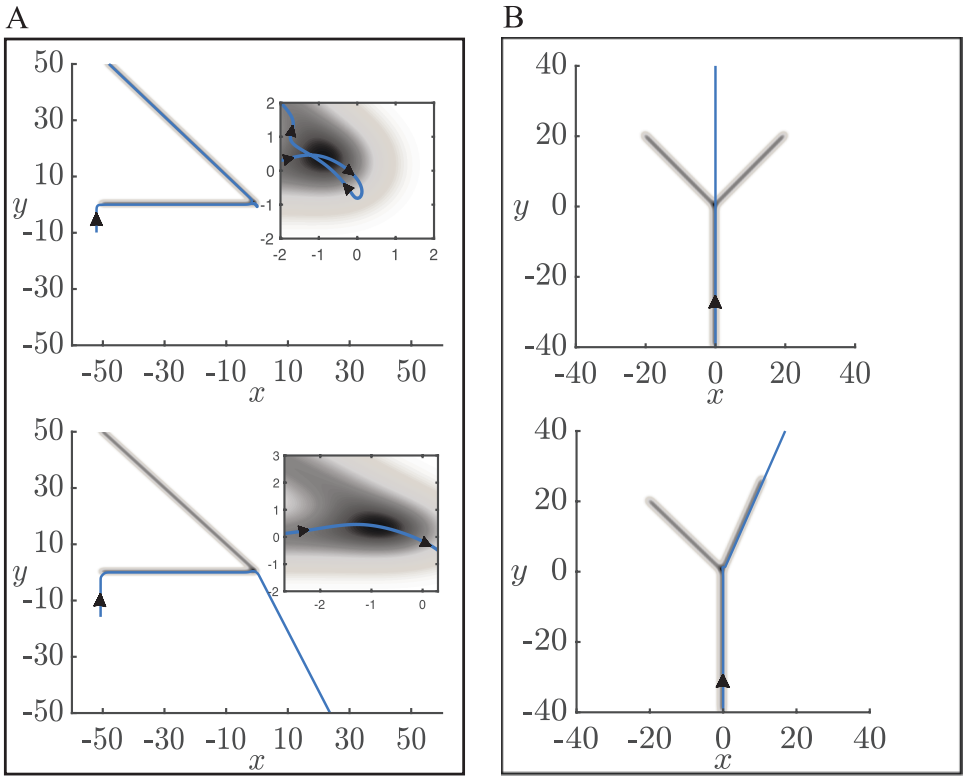

Fig. 16 (A) *(top) Trail with angle very close to but greater than* $\frac{\pi}{4}$*, zoomed in on how the model is able to correct and find the trail. (bottom) Trail with angle equal to* $\frac{\pi}{4}$*, zoomed in on how the model cannot sense the change in the angle and loses the trail.* (B) *(top) Y trail where the branches are at equal angles from the main trail. (bottom) Y trail where the branches are at different angles from the main trail. The blue line is a trajectory starting at the main trail.*

close spots (e.g., see Figure 11); otherwise the individual eventually reaches the end of the trail and moves away. Thus, in these cases, there are no attractors and basins, bifurcations, etc., do not make sense. We have included the results on branched and finite trails mainly because they provide for the possibility of experimentally testing some of the results. Indeed, some preliminary experiments in the lab of Nathan Urban examine the paths of mice that are trained to follow trails when the trails branch and have gaps.

7. Discussion. In this paper, we have analyzed a simplified dimensionless model that describes the use of bilateral information to navigate odor sources. We looked at how the model behaves in the presence of one or more odor spot sources, circular and infinite straight trails, and trails with gaps and angles. To allow for mathematical analysis of the model, some simplifications were applied. Instead of using a more realistic odor description such as turbulent plumes [7], we presented concentration as fixed Gaussian distributions. We also kept the function that determines the change in the heading angle linear in the difference between left and right concentrations unlike previous work [4, 5]. Calenbuhr et al. [4, 5] put the concentrations through a Michaelis–Menten type nonlinearity, so that saturation occurs at large concentrations.

These nonlinearities do not change the qualitative behavior (in fact, on an infinite trail, the fixed points are the same), but alter some of the details like the basin of attraction and the degree of multistability. Some animals change their velocities while searching for odor sources (for example, ants [9] and mice [18] decrease their velocity closer to the source); here, though, we did not take variable velocity into consideration. With our simplifications, we were able to examine how the performance changes as we vary different parameters. The main parameters we looked at in our scaled model are the length l of the sensors, the angle ϕ between the sensors, and the sensitivity β to concentration change.

In the case of the infinite line, as we increase β, both the analytical and simulated basins of attraction increase, which is expected since the change in heading angle becomes more sensitive to the concentration difference. When ϕ is larger or l is smaller, we see increased sinusoidal motion centered at the trail. When the odor source is a spot, one of the fixed points of the model is a saddle point and the other is unstable (at r close to 0). This suggests that the individual will not be able to find spot sources; however, we can see from the figures (in the (x, y)-plane) that trajectories pass through the spot. The reason that the model moves away from the spot is that we have required that the speed stay constant. When multiple spot odor sources are added, the (x, y, θ) system exhibits trajectories that pass through one source or multiple sources, periodic orbits around sources, and chaotic behavior. Because Gaussian circular trails share the radially symmetric property with single spots, we use the same (r, ξ) system to study how varying l, β, and ϕ affects its stability and basin of attraction on these trails. The fixed point (circular trail) becomes stable at a small radius ($r_0 \sim 0.5$) and remains stable for all larger radii. As in infinite trails, when we increase β on a circular trail with large enough radius, the basin of attraction increases. This is not true for smaller radii or when we increase the length of the nares l where an optimal length $l < r_0$ gives the largest basin of attraction. When the odor source is a finite straight trail, the individual will keep on the trail once it finds it, even if there is a gap because of the symmetry between the nares. If the trajectory is sinusoidal (see, e.g., Figure 15(B)), then the individual can lose the trail at the gap depending on the amplitude of the fluctuations. When there is a trail with an angle, the individual turns and keeps on the trail if the angle is larger than $\pi/4$, and loses the trail otherwise. If the trail bifurcates into two branches, we see that the individual chooses the branch with a smoother turn angle. This is seen in rats in [14], where they tended to choose the branch that had a smaller angle with the main trail (straighter).

At a fixed sensor length l, there is an angle ϕ that makes the system most stable and causes it to have an optimal basin of attraction when the odor landscape is an infinite line. For a spot source, we are also able to find an optimal ϕ by freezing the individual while orienting it toward the spot ($\xi = \pi$) and studying the linearization of the new system. We conclude that the individual will best reach the source if it keeps ϕ closer to zero when it is away from the spot and closer to $\pi/2$ (large sinusoidal behavior) when it is near the spot. This contradicts the best strategy that we have found to acquire and stay on an infinite trail, where it is better to have a smaller ϕ closer to the trail. This shows that animals consider different ways to optimize their search depending on the odor distribution. For example, similar to our results, in Draft et al. [9] ants move their antennas to have smaller angles while following the trail and bigger angles when exhibiting sinusoidal movements near the trail. In Khan, Sarangi, and Bhalla [14], rats were able to cross gaps and reacquire the trail by increasing the

amplitude of their head casting (which might suggest that they are using the strategy discussed to best find infinite trails by changing their method, since they cannot control the angle between nares). Also, in Liu et al. [18], mice exhibit an increase in sinusoidal behavior near the spot source and their trajectories become more tortuous.

Real odor landscapes are not simple smooth gradients, but rather temporally complicated and turbulent. In Boie et al. [2], the authors showed that the spatial information provided by the two sensors is nonredundant in turbulent plumes. We have tested the simple bilateral algorithm in a plume (not shown here) and we observed that the individual can successfully find the odor source. Similar to our previous results, we have to start at a position orienting toward the plume in order to find it because we do not add noise or a corrective method to turn the individual back once it veers off the plume. One major aspect that we have not explored in this paper is the effects of noise on the models. There are several ways we could introduce this variability in the model. For example, the odor concentration at a point in space could be converted to a rate for a Poisson process and the number of hits in some window of time could act as the main signal. In other work [18], we have used this type of model to mimic the behavior of mice looking for spots of odor. Another type of stochasticity that could be included is additive noise in the equation for θ. That is, in the absence of any odor cue, the individual undergoes a correlated random walk. Such behavior is commonly seen as a foraging strategy for animals and in the present case would have the effect of allowing the individual to correct for starting conditions that, in the deterministic case, would lead it away from the odor source. Whether there is an optimal amount of such "noise" to maximize the probability of success is currently a subject of further research. The bilateral model explains many results observed in animal data, but not all behavior. Understanding the underlying dynamics of the bilateral model will help in building models that use bilateral information together with other strategies such as casting or upwind orientation.

REFERENCES

[1] P. F. Beglane, F. W. Grasso, J. A. Basil, and J. Atema, *Far field chemo-orientation in the American lobster, Homarus americanus: Effects of unilateral ablation and lesioning of the lateral antennule*, Biol. Bull., 193 (1997), pp. 214–215, https://doi.org/10.1086/BBLv193n2p214. (Cited on p. 101)

[2] S. D. Boie, E. G. Connor, M. McHugh, K. I. Nagel, G. B. Ermentrout, J. P. Crimaldi, and J. D. Victor, *Information-theoretic analysis of realistic odor plumes: What cues are useful for determining location?*, PLoS Comput. Biol., 14 (2018), pp. 1–19, https://doi.org/10.1371/journal.pcbi.1006275. (Cited on p. 119)

[3] A. Borst and M. Heisenberg, *Osmotropotaxis in Drosophila melanogaster*, J. Comparative Physiol., 147 (1982), pp. 479–484, https://doi.org/10.1007/BF00612013. (Cited on p. 101)

[4] V. Calenbuhr, L. Chrétien, J.-L. Deneubourg, and C. Detrain, *A model for osmotropotactic orientation* (II), J. Theoret. Biol., 158 (1992), pp. 395–407, https://doi.org/10.1016/S0022-5193(05)80739-8. (Cited on pp. 101, 117)

[5] V. Calenbuhr and J.-L. Deneubourg, *A model for osmotropotactic orientation* (I), J. Theoret. Biol., 158 (1992), pp. 359–393, https://doi.org/10.1016/S0022-5193(05)80738-6. (Cited on pp. 101, 117)

[6] K. C. Catania, *Stereo and serial sniffing guide navigation to an odour source in a mammal*, Nature Commun., 4 (2013), art. 1441. (Cited on p. 101)

[7] E. G. Connor, M. K. McHugh, and J. P. Crimaldi, *Quantification of airborne odor plumes using planar laser-induced fluorescence*, Exp. Fluids, 59 (2018), art. 137, https://doi.org/10.1007/s00348-018-2591-3. (Cited on p. 117)

[8] C. Derby, P. Steullet, A. J. Horner, and H. Cate, *The sensory basis to feeding behaviour in the Caribbean spiny lobster Panulirus argus*, Mar. Freshwater Res., 52 (2001), pp. 1339–1350, https://doi.org/10.1071/MF01099. (Cited on p. 101)

[9] R. W. Draft, M. R. McGill, V. Kapoor, and V. N. Murthy, *Carpenter ants use diverse antennae sampling strategies to track odor trails*, J. Exp. Biol., 221 (2018), art. 185124, https://doi.org/10.1242/jeb.185124. (Cited on p. 118)

[10] B. J. Duistermars, D. M. Chow, and M. A. Frye, *Flies require bilateral sensory input to track odor gradients in flight*, Current Biol., 19 (2009), pp. 1301–1307, https://doi.org/10.1016/j.cub.2009.06.022. (Cited on p. 101)

[11] F. W. Grasso and J. A. Basil, *How lobsters, crayfishes, and crabs locate sources of odor: Current perspectives and future directions*, Current Opinion in Neurobiol., 12 (2002), pp. 721–727, https://doi.org/10.1016/S0959-4388(02)00388-4. (Cited on p. 101)

[12] W. Hangartner, *Spezifität und Inaktivierung des Spurpheromons von Lasius fuliginosus Latr. und Orientierung der Arbeiterinnen im Duftfeld*, Z. vergl. Physiol., 57 (1967), pp. 103–136, https://doi.org/10.1007/BF00303068. (Cited on p. 101)

[13] Y. Huang, J. Yen, and E. Kanso, *Detection and tracking of chemical trails in bio-inspired sensory systems*, European J. Comput. Mech., 26 (2017), pp. 98–114, https://doi.org/10.1080/17797179.2017.1321207. (Cited on p. 101)

[14] A. G. Khan, M. Sarangi, and U. S. Bhalla, *Rats track odour trails accurately using a multi-layered strategy with near-optimal sampling*, Nature Commun., 3 (2012), art. 703, https://doi.org/10.1038/ncomms1712. (Cited on pp. 101, 118)

[15] S. Kikuta, K. Sato, H. Kashiwadani, K. Tsunoda, T. Yamasoba, and K. Mori, *Neurons in the anterior olfactory nucleus pars externa detect right or left localization of odor sources*, Proc. Natl. Acad. Sci. USA, 107 (2010), pp. 12363–12368, https://doi.org/10.1073/pnas.1003999107. (Cited on p. 101)

[16] G. Kowadlo and R. A. Russell, *Robot odor localization: A taxonomy and survey*, Internat. J. Robotics Res., 27 (2008), pp. 869–894, https://doi.org/10.1177/0278364908095118. (Cited on p. 101)

[17] A. E. Leonard, R. Voigt, and J. Atema, *Lobster orientation in turbulent odor plumes: Electrical recording of bilateral olfactory sampling (antennular "flicking")*, Biol. Bull., 187 (1994), p. 273, https://doi.org/10.1086/BBLv187n2p273. (Cited on p. 101)

[18] A. Liu, A. E. Papale, J. Hengenius, K. Patel, B. Ermentrout, and N. N. Urban, *Mouse navigation strategies for odor source localization*, Frontiers Neurosci., 14 (2020), p. 218, https://doi.org/10.3389/fnins.2020.00218. (Cited on pp. 118, 119)

[19] H. Martin, *Osmotropotaxis in the honey-bee*, Nature, 208 (1965), pp. 59–63, https://doi.org/10.1038/208059a0. (Cited on p. 101)

[20] A. P. Nosal, Y. Chao, J. D. Farrara, F. Chai, and P. A. Hastings, *Olfaction contributes to pelagic navigation in a coastal shark*, PLoS ONE, 11 (2016), pp. 1–17, https://doi.org/10.1371/journal.pone.0143758. (Cited on p. 101)

[21] J. Porter, T. Anand, B. Johnson, R. M. Khan, and N. Sobel, *Brain mechanisms for extracting spatial information from smell*, Neuron, 47 (2005), pp. 581–592, https://doi.org/10.1016/j.neuron.2005.06.028. (Cited on p. 101)

[22] J. Porter, B. Craven, R. M. Khan, S.-J. Chang, I. Kang, B. Judkewitz, J. Volpe, G. Settles, and N. Sobel, *Mechanisms of scent-tracking in humans*, Nature Neurosci., 10 (2007), pp. 27–29. (Cited on p. 101)

[23] R. Rajan, J. P. Clement, and U. S. Bhalla, *Rats smell in stereo*, Science, 311 (2006), pp. 666–670, https://doi.org/10.1126/science.1122096. (Cited on pp. 100, 101)

[24] P. B. Reeder and B. W. Ache, *Chemotaxis in the Florida spiny lobster, Panulirus argus*, Animal Behaviour, 28 (1980), pp. 831–839, https://doi.org/10.1016/S0003-3472(80)80143-6. (Cited on p. 101)

[25] T. C. Schneirla, *A unique case of circular milling in ants, considered in relation to trail following and the general problem of orientation*, Amer. Museum Novitates, no. 1253 (1944), pp. 1–26. (Cited on p. 112)

[26] M. Vergassola, E. Villermaux, and B. I. Shraiman, *"Infotaxis" as a strategy for searching without gradients*, Nature, 445 (2007), pp. 406–409. (Cited on p. 102)